Journal of Applied Fluid Mechanics, Vol. 17, No. 7, pp. 1514-1523, 2024.
Available online at www.jafmonline.net, ISSN 1735-3572, EISSN 1735-3645.
https://doi.org/10.47176/jafm.17.7.2328

Research on Separation Loss of Compressor Cascade Profile Based on Large Eddy Simulation

X. Li, Q. Zheng, Z. Chi and B. Jiang†

Turbomachines Laboratory, Department of Power and Energy Engineering, Harbin Engineering University, Harbin, 150000, China

†Corresponding Author Email: jiangbin_hrbeu@163.com

ABSTRACT

The boundary layer's separation loss in compressor cascades constitutes a significant portion of profile loss, critically influencing aerodynamic performance optimization and control. This study employs Large Eddy Simulation (LES) to examine separation losses at varying attack angles, focusing on a rectangular compressor cascade. Specifically, it explores the long separation bubble at a 45% blade height cross-section under designed incidence. Analysis of the separation bubble's transition process revealed a notable surge in total pressure loss rate prior to transition, which stabilized following reattachment. The study thoroughly investigates the evolution of long bubbles, employing quadrant analysis of Reynolds stress, critical point theory, and an in-depth examination of individual vortex dynamics. The findings indicate that the peak of cross-flow within the separation bubble acts as the primary mechanism initiating the transition. This insight is corroborated by DNS calculations of natural transitions on flat plates. Building upon these findings, the study discusses the effects of varying attack angles on transition processes. Notably, increased incidence prompted the upstream migration of the long separation bubble, transforming it into a short bubble at the leading edge. This shift led to a fivefold increase in separation loss and doubled the frequency of transverse flow fluctuations.

Article History

Received September 24, 2023
Revised January 12, 2024
Accepted February 3, 2024
Available online April 30, 2024

Keywords:

Large eddy simulation
Compressor cascade
Transition
Separation bubble
Separation loss
Cross flow
Spiral point

1. INTRODUCTION

Separation loss within cascade flows is a critical component of profile loss. It arises from boundary layer disruptions and wake phenomena occurring at mid-span, distinct from the end-wall (Lee et al., 2020). Profile loss is predominantly analyzed in the context of a two-dimensional blade cross-section, particularly in scenarios with high aspect ratios (Gostelow et al., 2013). The intricate nature of flow behavior presents challenges in accurately quantifying profile losses, especially those attributable to boundary layer separation (Denton 1993; Wang et al., 2020).

Elevated loading conditions induce stronger counter-pressure gradients, which in turn lead to the formation of laminar separation bubbles (Scillitoe et al., 2016). These bubbles, known for their periodic formation and collapse, contribute to additional aerodynamic blockage (Michael et al., 2010). At low levels of incoming flow turbulence, the Kelvin-Helmholtz (K-H) instability predominates (Hosseinverdi & Fasel 2019). However, with an increase in incoming flow turbulence, the K-mode instability becomes more significant.

The loss mechanism on the suction side of the blade represents a complex, three-dimensional challenge. Notably, cross-flow is prevalent in cascades away from the end-wall, primarily due to a strong radial component in the streamlines (Gostelow et al., 2013). Theoretical models suggest that as cross-flow waves amplify downstream, they alter the span-wise chord-wise mean velocity profile. A key characteristic of this phenomenon is the flow cross-flow vortices induced by free-stream turbulence (Schrader et al., 2010). The role of cross flow in the airfoil boundary layer is pivotal and has been the subject of extensive research (Itoh 1996).

Currently, the impact of cross-flow on separation loss necessitates additional theoretical investigation. Progress in understanding transition mechanisms within three-dimensional boundary layers can be categorized into external and internal flows.A shared characteristic in both categories is the identification of cross-flow as the flow perpendicular to the main flow direction. The transition begins when the average velocity profile becomes distorted. In external flows, like those over aircraft surfaces and elliptical cones, the boundary layer displays significant three-dimensional traits that can give rise to cross-flow instabilities (Zhu et al., 2022). Research by

NOMENCLATURE

$\langle u_i' \ u_k' \rangle$	Reynolds stress	H	Helicity
htotal	total enthalpy	TKE	Turbulent Kinetic Energy
Pabs	absolute pressure	i	time index during navigation
C	axial chord length	Cp	Total pressure coefficient
P_{in}	static pressure at the inlet	P_k	rate of turbulence production
k'	pulsation kinetic energy		

Poll (1985) explored the downstream amplification of swept-plate flow cross-flow waves. These waves can alter the chord-wise mean velocity profile in the span-wise direction and are susceptible to high-frequency secondary instabilities. In the realm of internal flows, cross-flow engenders a complex array of impacts on engine performance. For example, during near-instability conditions in compressors, the low-speed fluid on the suction surface amalgamates with the tip leakage vortex, intensifying blockages (Horlock et al., 1974). The methodology of integrating co-flow and cross-flow boundary layer profiles in turbo-machinery has been well established (Hall et al., 1984).

Reference (Yaras 2011) examined the influence of cross-flow on the instability of the upstream boundary layer, including its impact on transition onset and rate within the separation bubble. The cross-flow pressure field arises both in the laminar boundary layer upstream of the separation and within the separation bubble itself. Cross-flow within the boundary layer induces asymmetric development in dominant flow characteristics (Giulia et al., 2022). The nonlinear interaction with the steady cross-flow vortex alters the mean flow (Han et al., 2019), while the proliferation of high-frequency secondary destabilizing waves contributes to the disintegration of the cross-flow vortex structure, ultimately precipitating the transition.

The conventional γ-θ model is less effective in predicting cross-flow transitions compared to the enhanced γ-θ-C1 model. Building on previous research, the C1 transition model demonstrates a separation bubble transition that most closely aligns with LES findings (Li. et al., 2024). This paper delves into the separation loss of compressor cascade profiles by theoretically examining the cross-flow-induced separation bubble transition. Initially, the evolution of the helical node is determined through Reynolds stress $\langle u_j' u_k' \rangle$ analysis and local streamline evaluation, which is then compared with the natural transition observed in flat plate experiments. Subsequently, this study examines the fluctuation traits of the separation bubble and cross-flow under varying attack angles, which culminates in an analysis of the unsteady factors contributing to this phenomenon.

2 LARGE EDDY SIMULATION AND ANALYSIS METHOD

2.1 Solution Method

The focus of this research is a rectangular cascade configured using the blade shape. This blade shape represents 50% of the blade height of a mid-stage, low-turning-angle stator blade in a multi-stage axial flow compressor. The parameters are detailed in Table 1. The incidences are set at -4°, 0°, 4°, 10°, and 18°, with consistent Mach numbers (Ma) across these incidences.

Table 1 Model Parameters

Consistency	1.05
Blade height/(mm)	100
Chord length/(mm)	70
Airflow turning angle/(°)	21.5
Outlet airflow angle/(°)	20
Reynolds number	3.26×10^5
Mach number	0.2
Outlet pressure/(Pa)	96900.5

Our team conducted wind tunnel experiments and visualization studies on the cascade (Li. et al., 2024), finding that the LES results at 0° incidence align well with experimental data. The boundary conditions for other angles of attack in this study are based on experimental measurements, lending credibility to the LES's prediction of flow details.

The instantaneous equations for mass, momentum, and energy conservation are presented in a stationary frame as follows:

$$\frac{\partial \rho}{\partial t} + \frac{\partial}{\partial x_j}\left(\rho U_j\right) = 0 \tag{1}$$

$$\frac{\partial}{\partial t}\left(\rho U_i\right) + \frac{\partial}{\partial x_j}\left(\rho U_j U_i\right) = -\frac{\partial p}{\partial x_j} + \frac{\partial}{\partial x_j}\left[\mu\left(\frac{\partial U_i}{\partial x_j} + \frac{\partial U_j}{\partial x_i}\right)\right] \tag{2}$$

$$\frac{\partial(\rho h_{\text{total}})}{\partial t} - \frac{\partial p}{\partial t} + \nabla \cdot (\rho U h_{tot}) = \nabla \cdot (\lambda \nabla T) + \nabla \cdot (U \cdot \tau) \tag{3}$$

Where, h_{total} represents the total enthalpy, and the term $\nabla (U \cdot \tau)$ denotes the work attributable to viscous stresses. For an ideal gas, the equation is:

$$\rho = \frac{wP_{abs}}{R_0 T} \tag{4}$$

Where, w denotes the molecular weight, P_{abs} represents the absolute pressure, and R_0 represents the universal gas constant.

A wall-adapted local eddy viscosity model (LES WALE model) is utilized. The WALE models are advantageous due to their ability to constrain subgrid-scale (SGS) viscosity in laminar flows. This makes them more apt for modeling separation bubble flows compared to existing models (Scillitoe et al., 2016). A central differential scheme with second-order accuracy is employed, aiming for a converged residual of less than 1 times 10^{-6}. The computational time step is set at 7.5 times 10^{-7} seconds, maintaining a Courant number of 0.44 throughout the calculations. The total CPU time amounted to 2.68 times 10^8 seconds, covering 60000×5 calculation steps, equivalent to a flow distance of 54 times the chord length.

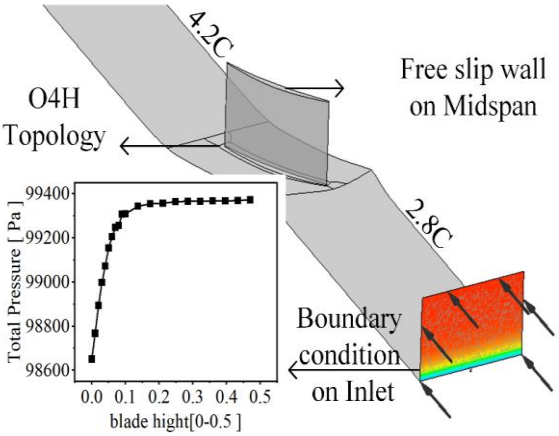

Fig. 1 Inlet Boundary Conditions

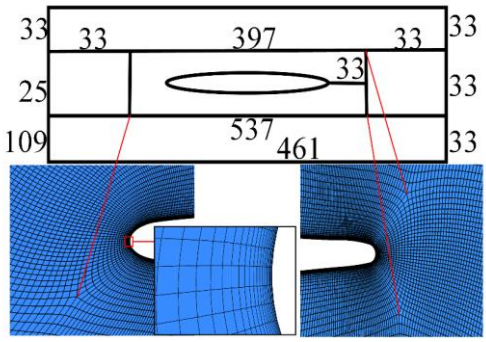

Fig. 2 Mesh Quality

This case focuses on the loss near the middle of the blade (45% h), while also accounting for the end-wall and corner regions. Inclusion of end walls in the calculations is crucial as it enables the consideration of radial flow, which is fundamental for assessing cross-flow instability mechanisms. The inlet flow is set at 2.8 C (2.8 times the axial chord length), with the outlet flow at 4.2 C.

At the inlet boundary, total pressure, total temperature, and the angle of the incoming flow are specified. To accurately assess cross-flow, a calculation incorporating an end wall is conducted, capturing flow details across all end-wall surfaces and corner areas. The single-channel model employs periodic boundary conditions on both sides, with non-slip walls at the hub and blade and a slip boundary condition at the mid-span. The inlet boundary conditions are depicted in Fig. 1.

The O4H grid's node count is presented in Fig. 2. The grid for the boundary layer thickness comprises 33 layers, amounting to a total of 2.9×10^7 grids. The grid nodes in the first layer adhere to the quality criteria of Y+<1, X+<40, and Z+<40.

2.2 Explanation of the Quadrant Analysis Method

Quadrant analysis is an established method in turbulence research commonly employed for investigating the generation of Reynolds stress (Freidoonimehr et al., 2024) and the characteristics of coherent structures (Mangan et al., 2023; Shig et al., 2023). When conducting

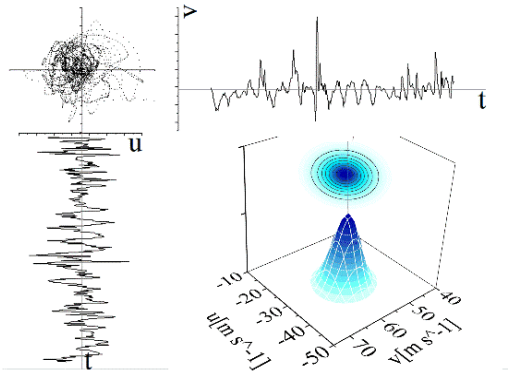

Fig. 3 Joint Probability Density Distribution of Monitoring Points in the Turbulent Boundary Layer

quadrant analysis on Reynolds stress within the airfoil's disturbed flow field—a complex, interconnected area, it is essential to transform coordinates within the global system. For Reynolds stress monitoring, auto-correlation at a single spatial point is utilized instead of spatial correlation at various points along the mainstream direction. Figure 3 illustrates the velocity fluctuations of transverse and axial velocities post-convergence observed within the turbulent boundary layer. If the axis slope of the cloud image projection ellipse is negative, it indicates turbulent flow events like sweeps and ejections. Conversely, a positive slope denotes inward or outward motion.

The outward normal direction of the wall is considered positive, allowing decomposition into four quadrants based on the correlation coefficient's sign. In the first quadrant (Q1 event), with outward events, $\langle u' \rangle$ >0 and $\langle v' \rangle$ >0 are observed. Conversely, in the second quadrant (Q2), featuring ejection events, $\langle u' \rangle$ <0 and $\langle v' \rangle$ >0, the third (Q3) and fourth quadrants (Q4) correspond to inward and sweep events, respectively. The Reynolds stress transport equation for mean motion in incompressible flow is represented as:

$$\underbrace{\frac{\partial k}{\partial t}+\langle u_k\rangle\frac{\partial k}{\partial x_k}}_{c_k}=\underbrace{-\langle u_i'u_k'\rangle\frac{\partial\langle u_i\rangle}{\partial x_k}}_{P_k})-$$

$$\underbrace{\frac{\partial}{\partial x_k}\left(\frac{\langle p'u_k'\rangle}{\rho}+\langle k'u_k'\rangle-\nu\frac{\partial k}{\partial x_k}\right)}_{D_k}-\underbrace{\nu\frac{\partial u_i'}{\partial x_k}\frac{\partial u_i'}{\partial x_k}}_{\varepsilon} \quad (5)$$

Where, $k'=\langle u_i'u_i'\rangle/2$ represents the pulsation kinetic energy, and P_k represents the rate of turbulence production from the mean flow. Reynolds stress represents the average energy transfer to turbulent fluctuations through the rate of deformation in average motion. This is known as the turbulent kinetic energy generation term. In Equation (5), the sign of turbulent kinetic energy generation is determined by the interaction between S_{jk} and $\langle u_j'u_k'\rangle$.When term(ε) is evaluated from measured mean velocity gradients, it is found to be several orders of magnitude less than the deformation work term P_k. Consequently, deformation work, or turbulence production, predominantly contributes to total pressure loss. Positive values indicating this phenomenon have been observed in various studies (Moore & Adhye 1985; Sharma & Butler, 1987; Gregory et al., 1988; Harrison 1990; Popovic, 2005). Negative values, conversely, signify the rate at which mean kinetic energy is converted into

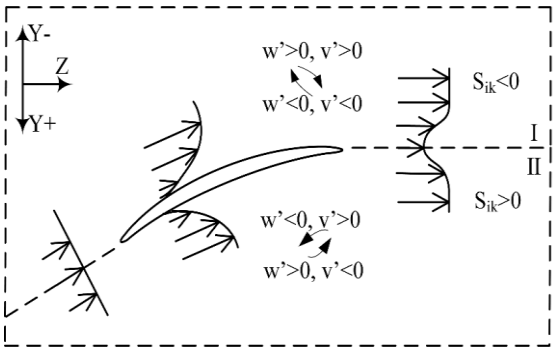

Fig. 4 Sign Rules for Quadrant Analysis in Different Regions

turbulence, leading to a loss in total pressure. When $P_k > 0$, the average motion inputs energy to the pulsatile motion. Generally speaking, $\langle u_j' u_k' \rangle$ is usually negative when the S_{jk} of average motion is positive, suggesting that Reynolds deviatoric stress mainly amplifies turbulent kinetic energy. This represents an energy loss that is not dissipated as heat but transformed into other forms (Zou et al., 2013).

The contribution of sweep and ejection events to turbulence generation hinges on the sign of Reynolds deviatoric stress and S_{jk}. As illustrated in Fig. 4, the outward normal direction on the suction surface side is negative. Therefore, the quadrant analysis for the suction surface indicates that upward spraying and downward sweeping correspond to $\langle u_j' u_k' \rangle > 0$, so that $P_k > 0$ results in an increase in turbulent kinetic energy. On the pressure side, the standard rules are applicable. The analysis clarifies the role of sweep and ejection events, distinct from Q2/Q4 events, to avoid confusion.

3 SEPARATION LOSS AT DESIGNED INCIDENCE

The separation loss in airfoils, particularly away from the end wall, is primarily due to the separation bubble. This study focuses on the 45% blade height plane, and discusses the separation loss of the boundary layer at the design incidence, with a specific emphasis on the relationship between separation loss and the transition of the separation bubble.

3.1 Losses Caused by the Separation Bubble

To analyze the separation loss before and after transition, the channel loss at each position of the design incidence is presented. Figure 5 illustrates the Cp and its first derivative. The static pressure coefficient is defined as follows:

$$\mathrm{Cp} = \frac{P - P_{in}}{(\frac{1}{2}\rho v^2)_{in}} \tag{6}$$

Where, P_{in} and $(\frac{1}{2}\rho v^2)_{in}$ denote the static pressure at the inlet and the static pressure, respectively. At an incidence of 0°, the presence of a long bubble leads to a transitional phenomenon. This long separation bubble shear layer is divided by the transition point into a laminar boundary layer and a transitional boundary layer (Li et al., 2024). Among various methods to determine the transition

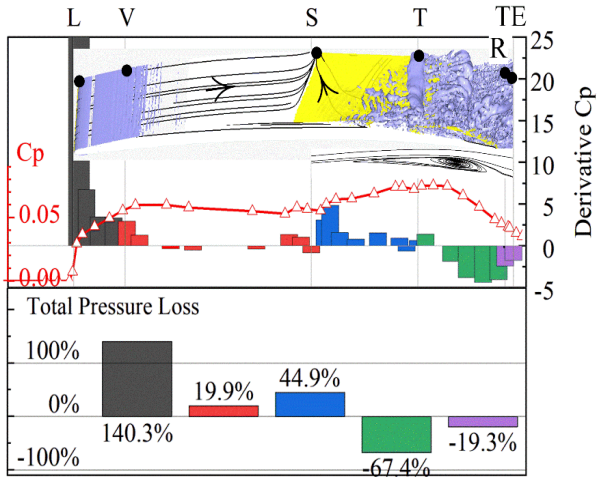

Fig. 5 Total Pressure Loss and Proportion of the Boundary Layer at 45% Blade Height

point, a significant decrease in helicity serves as a key indicator (Xu et al., 2016). Vortex tube rupture occurs where helicity drops from the transition point T, approximately at the midpoint of the separation bubble. The total pressure loss in the cascade passage varies significantly across different regions. Figure 5 categorizes the channel into distinct stages along the flow direction, marked by specific points: Leading Edge Point (L), Leading Edge Viscosity Loss Point (V), Separation Point (S), Transition Point (T), Reattachment Point (R), and Trailing Edge Point (TE). The total pressure loss is the circumferential average value calculated along a straight line through each point at 45% H. It is noteworthy that the loss on the suction side is significant, as the pressure side's boundary layer remains laminar without a separation bubble.

As depicted in Fig. 5, viscous loss is most prominent near the leading edge, with the laminar flow separation bubble from S to T following closely. The proportion of laminar loss is minor, but the rate of total pressure loss begins to escalate from separation point S. In the T-R zone and the wet zone, total pressure recovery occurs as the transition of the separation bubble enhances the adhesion of the boundary layer.

The long separation loss in the first half of the separation bubble accounts for 44.9% of the channel loss, while the total pressure recovery in the second half is 67.4%. Consequently, the overall impact of the separated bubbles facilitates total pressure loss recovery.

The transition point serves as a critical boundary between total pressure loss and recovery. Consequently, accurately pinpointing the onset of transition is essential for determining separation loss.

The generation of turbulent kinetic energy, as indicated in Equation (5), is a combined function of S_{jk} and $\langle u_j' u_k' \rangle$. Figure 4 demonstrates that on the suction side, with $S\{jk\} < 0$ and $P_k > 0$ when $\langle u_j' u_k' \rangle$ shifts from a negative to a positive position, there is a marked increase in turbulent kinetic energy, coinciding with the occurrence of ejection and sweep events (burst), as shown in Fig. 3.1.2. In this case, the typical conclusion is reversed. This is attributed to the orientation of the coordinate axis, where the $\langle u_j' u_k' \rangle$-axis, representing ejection and sweep events, predominantly lies in the first and fourth quadrants.

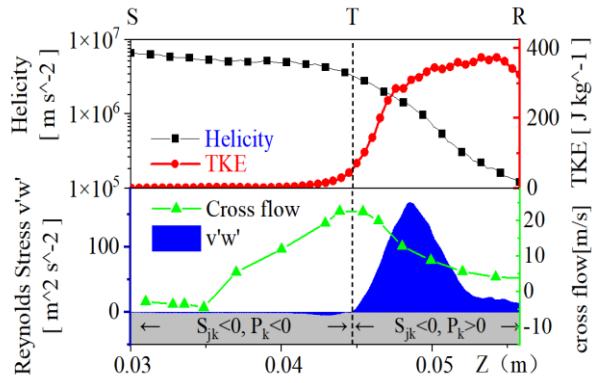

Fig. 6 Transition Parameters of the Separation Bubble for the Design Incidence

Helicity ($H = \omega \cdot v$) is directly influenced by the velocity along the vortex axis. At the 45% blade height cross-section, helicity and cross-flow variation characteristics in the flow direction are identified by their maximum wall-normal values. As indicated in Fig. 6, helicity decreases at point T, where cross-flow reaches its peak. It is important to note that the disappearance of loss correlates with the peak of Reynolds stress, transitioning from negative to positive. Furthermore, Fig. 5 suggests that the energy lost in separation (S-T) is not immediately converted into turbulent kinetic energy (TKE) but is stored in the rotational kinetic energy of the separation vortex in the S-T segment or in the viscous dissipation within the same segment. The breakdown of the long bubble begins its dissipation downstream of point T.

In summary, at 0°, the separation bubble facilitates the recovery of total pressure loss. When comparing helicity and turbulent kinetic energy, the peak of cross-flow more accurately locates the transition position of the long separation bubble.

3.2 Cross-Flow Transition

This section delves into the evolution of the separation bubble, from convergence to diffusion, to further explain the transition mechanism triggered by the cross-flow peak within the bubble. Initially, the laminar and turbulent flow regions are distinguished by analyzing the Reynolds stress $\langle u_j' u_k' \rangle$ quadrant (Fig. 7). Subsequently, the node pattern of each region is identified using the local streamline method.

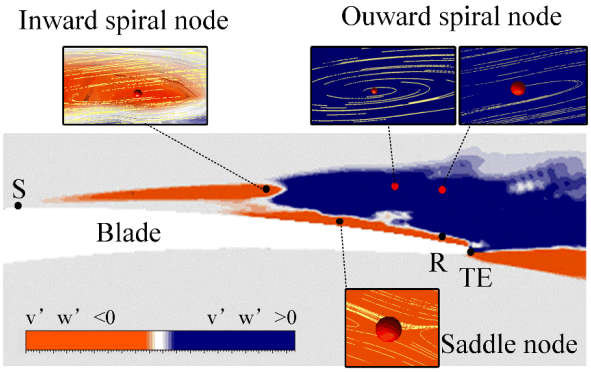

Fig. 7 Correlation between Node Pattern and Reynolds Stress

Vortices are generally perceived as rotating flows, yet their specific areas remain undefined. In compressor cascades, small-scale turbulent vortices are prevalent, but understanding the ubiquitous presence of separation bubbles in these cascades requires a comprehensive grasp of individual vortex evolution. The study by Zhang (1997) outlines the overall development of a vortex based on a local coordinate system. Keeping the axial velocity direction constant, the vortex development process is categorized into three stages: 1. The converging segment (stable spiral point), characterized by increasing axial velocity; 2. the point of maximum axial velocity (central point); 3. The diffusing segment (unstable spiral point), marked by decreasing velocity.

To observe the convergence and diffusion within the separation bubble, correlating boundary layer flow with critical point patterns is vital. Two-dimensional critical point theory is applied to evaluate stability characteristics. Existing literature (Zou et al., 2021) considers the analysis of local instantaneous streamlines on the phase plane as a method for representing vortices. The relevant equation is as follows:

$$\frac{dx}{dt} = ax + by, \frac{dy}{dt} = cx + dy \tag{7}$$

Where a, b, c and d are the real elements of the velocity tensor matrix.

The characteristic equation is given by:

$$D(\lambda) = \lambda^2 + p\lambda + q = 0 \tag{8}$$

where,

$$p = -(a+d), q = ad - bc, \Delta = p^2 - 4q \tag{9}$$

If we establish a local coordinate system on fluid particles within the flow field, placing the origin at the singular point of these coordinates, two-dimensional critical point theory becomes locally applicable (Li et al., 2021; Zou et al., 2021). By subtracting the velocity at each point and establishing local coordinates, any point can be transformed into a singular point (Chenzhi et al., 2003).

Figure 7 examines whether the separation bubble's two-dimensional vortex tube follows a similar pattern. Post-transition, the region near the wall aligns with a saddle-node point, indicating the absence of rotation at the laminar flow's bottom. The Reynolds stress transitions from negative to positive in the outer layer, with all points being spiral nodes. The key difference lies in their rotation direction—whether inward or outward. This transition shifts the spiral node from stable to unstable forms, corresponding to the vortex's converging and diffusing stages, respectively. Reflecting on the cross-flow discussed in Section 3.1.2, it aligns with the three stages of vortex development mentioned. Hence, the emergence of a cross-flow peak is the direct trigger for the separation bubble transition.

Flows with identical swirl directions but varying radial flow directions are termed inward and outward spiral flows. In this case, the transition alters the separation bubble's internal and external rotation. Notably, this is not

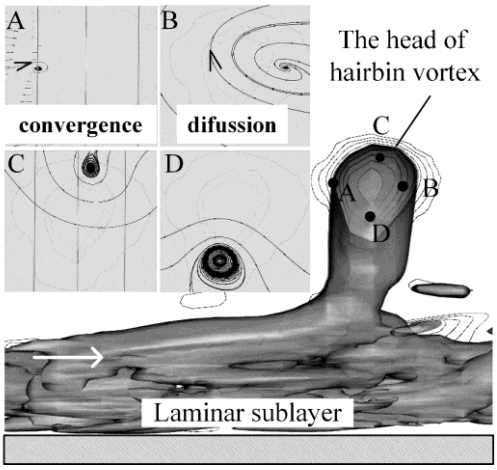

Fig. 8 Local Streamlines of a Natural Transition Hairpin Vortex in a Flat Boundary Layer

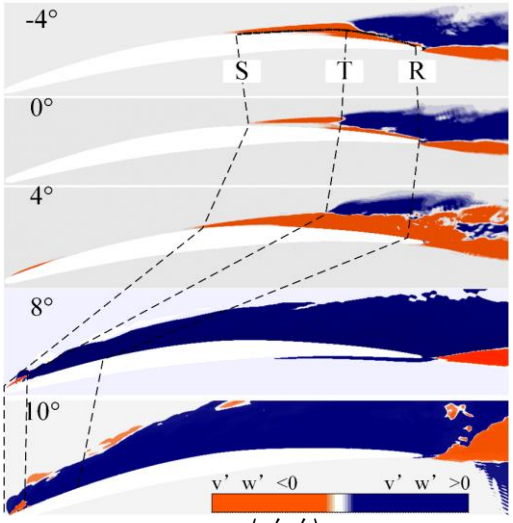

Fig. 9 Distribution of $\langle u_j' u_k' \rangle$ as a Function of Incidence

exclusive to separation bubble transition; the evolution process of the hairpin vortex in natural transition follows a similar pattern.

Figure 8 presents a side view of the hairpin vortex and the monitoring point at the vortex head. The hairpin vortex, observed in the natural transition of flat plate boundary layers, stems from the public DNS results by Liu's team (Jianming & Chaoqun, 2019 ; Gao et al., 2019; Xu et al., 2019; Wang et al., 2020). Using vortex identification technology like Liutex (Jianming et al., 2019) and local streamline analysis (Zou et al., 2021), it was found that the hairpin vortex heads sequentially evolve from inward spiral nodes to central nodes, then to outward spiral nodes. Thus, the patterns of local streamline changes in natural and separation bubble transitions are consistent: transitions shift spiral nodes from stable (inward rotation) to unstable (outward rotation), or, in simpler terms, from convergent pre-transition to divergent post-transition.

In summary, at the designed incidence, the separation loss of the airfoil originates from the converging section of the separation bubble, where cross-flow intensifies. The emergence of a cross-flow peak induces the transition from converging to diffusing within the separation bubble, culminating in the transition.

4 EFFECT OF INCIDENCE ON SEPARATION LOSS

It is known that the proportion of loss sources in a compressor cascade varies with incidence, with the accumulation of separation loss occurring between the separation point and the transition point. Utilizing the design incidence results, this section summarizes the characteristics of separation loss and its associated parameters, analyzing the underlying causes for these changes.

4.1 Variation of the Separation Bubble

Figure 9 illustrates how the position of the separation bubble shifts with varying incidence. It also provides a detailed analysis of the sign changes observed in Fig. 6. Typically, sweep and ejection events dominate in the turbulent boundary layer. However, characterizing the turbulence-dominated events prior to transition is challenging due to the rapid nature of bypass transitions.

In the cascade environment, the separation bubble delays and extends the transition process, stabilizing the flow and rendering the turbulent behaviors up to the transition stage more discernible. In this study, separation bubble transition phenomena are observed across a wide range of incidences. Figure 9 delineates the positive and negative $\langle u_j' u_k' \rangle$areas and traces the movement of S, T, and R points. The analysis ensures the Z-axis direction aligns with the tangential direction of point T, as $\langle u_j' u_k' \rangle$ is not Galileo invariant. The findings from Fig. 9 can be categorized into three distinct scenarios: 1. A long separation bubble (S-R) exists between -4° and 4°, with the length of the wet zone being almost negligible. 2. A shorter separation bubble is present between 4° and 10°, with the wet area extending from the reattachment point to the trailing edge (R-Tr). 3. Beyond 10°, the turbulent boundary layer undergoes another separation (S'-Tr), resulting in a shortened wet zone.

The convergence and diffusion of the separation bubble are represented by the orange and blue regions, respectively. This indicates that $\langle u_j' u_k' \rangle$ <0 in the S-T segment of both long and short bubbles signifies inward and outward movement events, while $\langle u_j' u_k' \rangle$ >0 in the outer layer of the T-R segment corresponds to sweep and ejection events. In all five examined cases, the separation bubble causes the boundary layer to stratify normally to the wall, indicating this stratification phenomenon as a universal occurrence. Replicating the quadrant analysis diagram is straightforward, provided the changes in coordinates are carefully considered. Ensuring that the flow direction aligns closely with the wall of the separation bubble is essential.

Figure 10 portrays three types of flows from -4° to 18° as schematic diagrams, taking into account the differences in separation loss caused by long and short separation bubbles. Based on the loss source proportions in Fig. 5, Fig. 10 summarizes the distribution of total pressure loss coefficients at each incidence.

As previously noted, the long separation bubble near the design incidence of the airfoil typically aids in total pressure recovery. At 8°, the chord-wise extent of the turbulent wet region is at its maximum, facilitating the greatest recovery of total pressure. The contribution of the wet zone to total pressure loss is predominantly negative

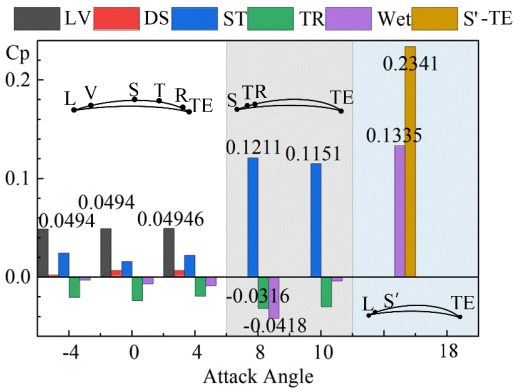

Fig. 10 Total Pressure Loss Coefficient at 45% Blade Height Section

before 10°, with the turbulent wet zone recovering total pressure before stalling. Post-10°, the turbulent boundary layer undergoes another separation, and the turbulent attachment area diminishes. At 18°, the turbulent flow's attachment area is confined to a short range near the leading edge. This suggests that post-stall, the leading edge transitions directly into a turbulent boundary layer, with the reattachment zone (wet zone) constituting 10% of the chord length and contributing 30% of the loss. The remaining 70% of the loss is attributed to the turbulent boundary layer separation region.

In summary, considering the overall contributions (S-T-R), the long bubble facilitates total pressure recovery, while the short bubble diminishes it. The separation loss of the short bubble (S-T section) is approximately five times greater than that of the long bubble.

4.2 Variation of Cross Flow

Evidence suggests that the emergence of a peak in cross flow at the design incidence is indicative of a separation bubble transition. To investigate the disparity in separation loss between long and short bubbles, the characteristics of the cross-flow peak in the S-T segment were analyzed and compared.

Figure 11 illustrates that the flow at the design incidence is optimal, exhibiting the lowest peak in turbulent kinetic energy (TKE) at 390 J/kg. The peak cross-flow velocity reaches 22.5 m/s, equivalent to 30% of the incoming flow. Here, incidences from -4° to 4° are collectively represented as 0°. At 10°, the cross flow sharply decreases to 6% of the incoming flow, with multiple peaks emerging, and the peak value of TKE is 2.5 times that of the design incidence. Even at stall incidence, a cross-flow-triggered transition occurs, but the appearance of the initial peak does not precisely correspond to the transition point. Due to the shortening of the separation bubble, a characteristic two-dimensional stratification becomes evident.

Separation losses are lower with single cross-flow peaks and higher with multiple peaks, possibly due to higher-frequency fluctuations in the short bubble.

Consequently, temporal fluctuations also reflect the cause of separation loss. Whether considering sound waves or fluid dynamics, it is recognized that higher frequencies dissipate more energy than lower frequencies. Analytical turbulence exhibits a broad-band spectrum, whereas the

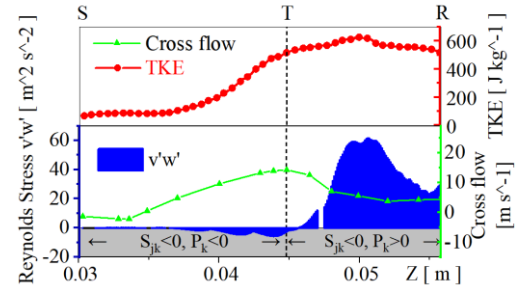

（a）-4°

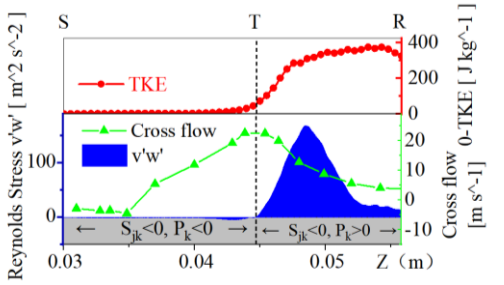

（b）0°

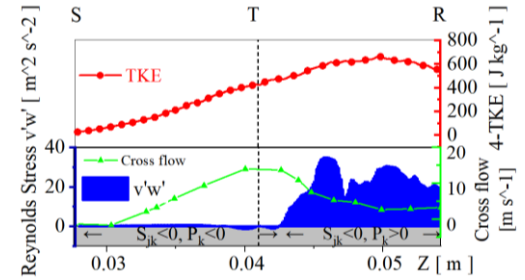

(c) 4°

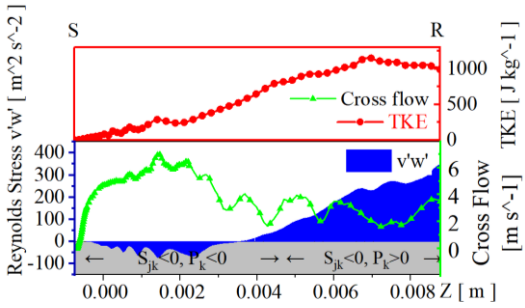

(d) 8°

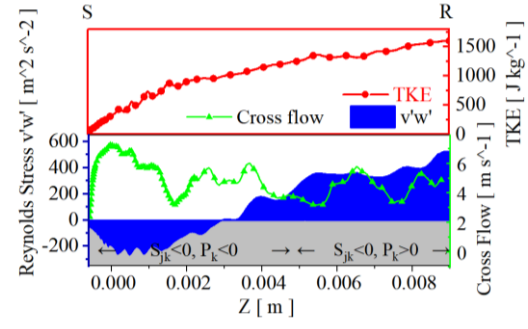

(e) 10°

Fig. 11 Parameter Changes of the Separation Bubble Transition

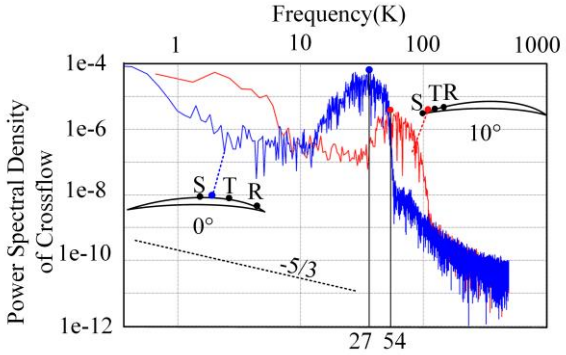

Fig. 12 Cross-Flow Velocity Spectrum of the Separation Bubble at 0°and 10°

transition point features a narrow-band spectrum. Figure 12 displays the cross-flow spectrum characteristics at the midpoint of the S-T segment, as well as the transition upstream points at 0° and 10°. Narrow-band features were also observed, enabling quantification of the cross-flow instability in the S-T segment.

This data indicates that the fluctuation frequency in the short bubble is twice that of the long bubble. This suggests that short-bubble cross-flow is characterized by a small scale and high fluctuation frequency, facilitating rapid energy exchange between the bubble and the main flow and resulting in greater separation loss.

In conclusion, the instabilities of separation bubble cross-flows intensify with increasing incidence. The high-frequency fluctuations of the short bubble at stall incidence are twice those of the long bubble, which significantly contributes to the fivefold increase in separation loss.

5 CONCLUSION

This study investigates the generation mechanism of airfoil separation loss in a rectangular cascade, yielding the following key conclusions:

An analysis of the total pressure loss rate was conducted along the chord-wise span of a large separation cell, located at 45% of the blade height, with the blade at 0° incidence. The findings reveal that the total pressure loss initially increases in the first half of the separation bubble. However, it then recovers in the latter half, using the onset of transition as the boundary.

It is demonstrated that the emergence of a peak in cross-flow is identified as the pivotal factor for the separation bubble transition. This finding is supported by quadrant analysis and local streamline analysis, which indicates that the cross-flow peak destabilizes the spiral point of the separation bubble. This destabilization causes the bubble to shift from convergence to diffusion, thereby triggering the transition.

In both long and short bubbles, the segment from the separation point to the transition point is a converging segment, predominantly characterized by inward and outward movement events. Conversely, the segment from the transition point to the reattachment point is a diffusing segment, dominated by sweep and ejection events.

The separation loss of the short bubble at the leading edge is approximately five times greater than that of the long bubble. Spatially, the cross-flow in the long bubble exhibits a singular peak, whereas the short bubble at the leading edge features multiple cross-flow peaks. Temporally, the instability of the separation bubble's cross-flow escalates with increasing incidence angles. This results in the high-frequency fluctuations of the short bubble at stall incidence being double that of the long bubble.

In the long separation bubble, the first half accounts for 44.9% of the channel's total loss, while the second half achieves a total pressure recovery of 67.4%. Consequently, the separation bubble at the design incidence negatively impacts total pressure loss, whereas the short bubble at the leading edge contributes positively to separation loss.

After the stall (at 18°), the wet zone, constituting 10% of the chord length, is responsible for 30% of the total loss. The remaining 70% of the loss originates from the turbulent boundary layer separation region.

ACKNOWLEDGEMENTS

The authors wish to thank the financial support of Harbin Engineering University. The DNS results of the boundary layer in this article come from Chaoqun Liu's team at the University of Texas at Arlington. Thanks for making the case public.

CONFLICT OF INTEREST

The authors have no conflicts to disclosure.

FUNDING

National Natural Science Foundation of China joint fund for regional innovation and development U20A20298 and National Science and Technology Major Project 2017-II-0006-0019.

AUTHORS CONTRIBUTION

Xiang Li: Writing – review & editing (lead); Conceptualization – Ideas (lead). **Qun Zheng**: Funding acquisition (lead); Supervision (equal); Resources; Conceptualization – Ideas (supporting). **Bin Jiang**: Supervision (equal); Resources (equal); Conceptualization – Ideas (supporting).

REFERENCE

Chengzhi, L., Li, W., & Zhang, Z. (2003). New families of centers and limit cycles for polynomial differential systems with homogeneous nonlinearities. *Annual Journal of Differential Equations: English Edition, 2003* (3), 302-317. https://api.semanticscholar.org/CorpusID:118427158

Denton, J. D. (1993). Loss Mechanisms in Turbomachines. *Proceedings of the ASME 1993 International Gas Turbine and Aeroengine Congress and Exposition. Volume 2: Combustion and Fuels; Oil and Gas Applications; Cycle Innovations; Heat Transfer; Electric Power; Industrial and Cogeneration; Ceramics; Structures and Dynamics; Controls, Diagnostics and Instrumentation;* IGTI Scholar Award. Cincinnati, Ohio, USA. May 24–27, 1993.

V002T14A001. ASME. https://doi.org/10.1115/93-GT-435

Freidoonimehr, N., Jafari, A., & Arjomandi, M. (2024). Characteristics of turbulent boundary layers generated by different tripping devices. *International Journal of Heat and Fluid Flow*, *105*, 109244. https://doi.org/10.1016/j.ijheatfluidflow.2023.109244

Gao, Y., Yu, Y., Liu, J., & Lou C. (2019). Explicit expressions for Rortex tensor and velocity gradient tensor decomposition. *Physics of Fluids*, *31*(8), 081704. https://doi.org/10.1063/1.5118948

Giulia, Z., Daniele R., Marios K. (2022). Transition due to isolated roughness in a swept wing boundary layer. *Physics of Fluids*, *34* (8), 084113. https://doi.org/10.1063/5.0101187

Gostelow, J. P., Rona, A., De Saint Jean, M., Garrett, S. J., & McMullan, W. A. (June 28, 2013). Investigation of Streamwise and Transverse Instabilities on Swept Cylinders and Implications for Turbine Blading. *ASME. Journal of Turbomachinery*, *135*(5): 051018. https://doi.org/10.1115/1.400783

Gregory-Smith, D. G., Graves, C. P., & Walsh, J. A. (1988). Growth of secondary losses and vorticity in an axial turbine cascade. *Journal of Turbomachinery*, *110*(1), 1–8. https://doi.org/10.1115/1.3262163

Hall, P., Malik, M. R., & Poll, D. I. A. (1984). On the stability of an infiniteswept attachment line boundary layer. *Proceedings of the Royal Society A: Mathematical, Physical and Engineering Science*, *395*, 229–245. https://doi.org/10.1098/rspa.1984.0099

Han, Y. F., Ma, S. X., & Su, C. H. (2019). Numerical study on crossflow transition in three-dimensiomal hypersonic boundary layers. Acta *Aerodynamica Sinica*, *37*(4),1092-1102. (in Chinese). https://doi.org/10.7638/kqdlxxb-2019.0015

Harrison, S. (1990). *Secondary loss generation in a linear cascade of high-turning turbine blades*. https://doi.org/10.1115/1.2927702

Horlock, J. H., & Perkins, H. J. (1974). Annulus wall boundary layers in turbomachines. https://api.semanticscholar.org/CorpusID:122452364

Hosseinverdi, S., & Fasel, H. F. (2019). Numerical investigation of laminar turbulent transition in laminar separation bubbles: The effect of free-stream turbulence. *Journal of Fluid Mechanics*, *858*, 714–759. https://doi.org/10.1017/jfm.2018.809

Itoh, N. (1996). Simple cases of the streamline-curvature instability in three-dimensional boundary layers. *Journal of Fluid Mechanics*, *317*, 129-154. https://doi.org/10.1017/S0022112096000699

Jianming, L., & Chaoqun, L. (2019). Modified normalized Rortex/vortex identification method. *Physics of Fluids 31* (6). 061704. https://doi.org/10.1063/1.5109437

Jianming, L., Yisheng, G., & C. Liu (2019). An objective version of the Rortex vector for vortex identification. *Physics of Fluids*, *31* (6), 065112. https://doi.org/10.1063/1.5095624

Lee, Y., Teramoto, S., Toki, T., & Okamoto, K. (2020). Effects of the large eddy simulation calculation parameters on prediction of profile loss in an axial cascade at off-design incidence. *Proceedings of the ASME Turbo Expo 2020: Turbomachinery Technical Conference and Exposition*. Volume 2C: Turbomachinery. Virtual, Online. September 21–25, 2020. V02CT35A011. ASME. https://doi.org/10.1115/GT2020-14554

Li, X., Zheng, Q., & Jiang, B. (2021). Mathematical Definition of Vortex Boundary and Boundary Classification Based on Topological Type. In: Skiadas, C.H., Dimotikalis, Y. (eds) *13th Chaotic Modeling and Simulation International Conference. CHAOS 2020. Springer Proceedings in Complexity*. Springer, Cham. https://doi.org/10.1007/978-3-030-70795-8_37

Li, X., Zheng, Q., Li, H., Yan, W., & Jiang, B. (2024). Numerical study of transition process in different zones of a compressor cascade channel. *International Journal of Turbo & Jet-Engines*, *40*(s1), s657-s669. https://doi.org/10.1515/tjj-2022-0084

Mangan, M. R., Oldroyd, H. J., Paw U, K. T., Clay, J., & Suvocarev, K. (2023). Evaluating the nature of turbulent coherent structures in orchards using integrated quadrant analysis. https://doi.org/10.2139/ssrn.4524630

Michael, G, List, Gorrell, S. E., & Turner, M. G. (2010). Investigation of loss generation in an embedded transonic fan stage at several gaps using high-fidelity, time-accurate computational fluid dynamics. *Journal of Turbomachinery*, https://doi.org/10.1115/1.3072522

Moore, J., & Adhye, R. Y. (1985). Secondary flows and losses downstream of a turbine cascade. *ASME. Journal of Engineering for Gas Turbines and Power*, *107*(4), 961–968. https://doi.org/10.1115/1.3239842

Poll, D. I. A. (1985). Some observations of the transition process on the windward face of a long yawed cylinder. *Journal of Fluid Mechanics*, *150*, 329-356. https://doi.org/10.1017/S0022112085000155

Popovic, I. (2005). *The Effects of leading edge geometry on profile and secondary losses in turbine cascades* [Master's thesis, Carleton University]. Ottawa, Canada.

Schrader, L. U., Amin, S., & Brandt, L. (2010). Transition to turbulence in the boundary layer over a smooth and rough swept plate exposed to free-stream turbulence. *Journal of fluid mechanics*, *646*, 297-325. (in Chinese). https://doi.org/10.1017/S0022112009993284

Scillitoe, A. D., Tucker, P. G., & Adami, P. (2016). Numerical Investigation of Three-Dimensional Separation in an Axial Flow Compressor: The Influence of Freestream Turbulence Intensity and Endwall Boundary Layer State. ASME. *Journal of Turbomachinery*, *139*(2): 021011. https://doi.org/10.1115/1.4034797

Sharma, O. P., & Butler, T. L. (1987). Predictions of endwall losses and secondary flows in axial flow turbine cascades. 1987. https://doi.org/10.1115/1.3262089

Shig, L., Babin, V., Shnapp, R., Fattal, E., Liberzon, A. & Bohbot, R. Y. (2023). Quadrant analysis of the reynolds shear stress in a two-height canopy. *Flow, Turbulence and Combustion*, 1-23. https://doi.org/10.1007/s10494-023-00421-6

Wang, M., Li, Z., Yang, C., Zhao, S., Zhang, Y., & Lu, X. (2020). Large eddy simulation of the separated flow transition on the suction surface of a high subsonic compressor airfoil. *Physics of Fluids*, *32*(3), https://doi.org/10.1063/1.5145068

Xu, J., Bai, J., Zhang, Y., & Qiao, L. (2016). Transition study of 3D aerodynamic configures using improved transport equations modeling. *Chinese Journal of Aeronautics*, *29*(4), 874-881. https://doi.org/10.1016/j.cja.2016.06.002

Xu, W., Gao, Y., Deng, Y., Liu, J., & Liu C. (2019). An explicit expression for the calculation of the Rortex vector. *Physics of Fluids*, *31*(9), 095102. https://doi.org/10.1063/1.5116374

Yaras, M. I. (2011). Instability and transition in a separation bubble under a three-dimensional freestream pressure distribution. *Journal of Turbomachinery*, https://doi.org/10.1115/1.4000533

Zhang, H. X. (1997). Crossflow topology of three dimensional separated flows and vortex motion. *Acta Aerodynamica Sinica*, *15*(1), 1-12. (in Chinese)

Zhu, Z., Feng, F., & Shen, Q. (2022). Large eddy simulation of hypersonic elliptical cone boundary layer transition characteristics. *Gas Physics*, *7*(3), 13. (in Chinese). https://pubs.cstam.org.cn/article/doi/10.19527/j.cnki.2096-1642.0950

Zoppini, G., Ragni, D., & Kotsonis, M. (2022). Transition due to isolated roughness in a swept wing boundary layer. *Physics of Fluids*, *34*(8), 084113. https://doi.org/10.1063/5.0101187

Zou, G., He, Z., & Gu, X. (2013). *Viscous fluid mechanics.* National Defense Industry Press. (in Chinese).

Zou, W., Xu, X., Tang, C. (2021). Spiral streamline pattern around a critical point: Its dual directivity and effective characterization by right eigen representation. *Physics of Fluids*, *33*(6), 067102. https://doi.org/10.1063/5.0050555